Excitations in the quantum paramagnetic phase of the quasi-one-dimensional Ising magnet $CoNb_2O_6$ in a transverse field: Geometric frustration and quantum renormalization effects

I. Cabrera, J. D. Thompson, R. Coldea, and D. Prabhakaran
Clarendon Laboratory, University of Oxford, Parks Road, Oxford OX1 3PU, United Kingdom

R. I. Bewley and T. Guidi
ISIS Facility, Rutherford Appleton Laboratory, Chilton, Didcot, Oxon OX11 0QX, United Kingdom

J. A. Rodriguez-Rivera and C. Stock
NIST Center for Neutron Research, National Institute of Standards and Technology, Gaithersburg, Maryland 20899, USA
(Received 2 April 2014; revised manuscript received 23 June 2014; published 15 July 2014)

The quasi-one-dimensional (1D) Ising ferromagnet $CoNb_2O_6$ has recently been driven via applied transverse magnetic fields through a continuous quantum phase transition from spontaneous magnetic order to a quantum paramagnet, and dramatic changes were observed in the spin dynamics, characteristic of weakly perturbed 1D Ising quantum criticality. We report here extensive single-crystal inelastic neutron scattering measurements of the magnetic excitations throughout the three-dimensional (3D) Brillouin zone in the quantum paramagnetic phase just above the critical field to characterize the effects of the finite interchain couplings. In this phase, we observe that excitations have a sharp, resolution-limited line shape at low energies and over most of the dispersion bandwidth, as expected for spin-flip quasiparticles. We map the full bandwidth along the strongly dispersive chain direction and resolve clear modulations of the dispersions in the plane normal to the chains, characteristic of frustrated interchain couplings in an antiferromagnetic isosceles triangular lattice. The dispersions can be well parametrized using a linear spin-wave model that includes interchain couplings and further neighbor exchanges. The observed dispersion bandwidth along the chain direction is smaller than that predicted by a linear spin-wave model using exchange values determined at zero field, and this effect is attributed to quantum renormalization of the dispersion beyond the spin-wave approximation in fields slightly above the critical field, where quantum fluctuations are still significant.

DOI: 10.1103/PhysRevB.90.014418 PACS number(s): 75.10.Jm, 75.10.Pq, 75.30.Ds

I. INTRODUCTION

Quantum phase transitions are characterized by a qualitative change in the ground state of a system that occurs upon varying an external parameter at zero temperature. The one-dimensional (1D) quantum Ising chain in transverse magnetic field is one of the most theoretically studied paradigms for a continuous quantum phase transition [1]. Here, a transverse magnetic field promotes quantum fluctuations in a ground state where spins are initially spontaneously ferromagnetically aligned "up" or "down" along an Ising axis. When these fluctuations are strong enough (compared to mean-field effects), the spontaneous Ising order is suppressed giving way to a quantum paramagnetic phase, where spins are in a correlated superposition of "up" and "down" states. Although this model was solved exactly more than four decades ago (via mapping to Jordan-Wigner fermions [2]), an experimental realization of this theoretical paradigm was only recently achieved [3] in the quasi-1D Ising-like ferromagnet $CoNb_2O_6$. Experiments observed that at a critical field applied transverse to the Ising axis, a phase transition occurred from the spontaneously ordered state, characterized by 1D domain-wall (kink) excitations, into the quantum paramagnetic phase, characterized by sharp, spin-flip quasiparticles. Moreover, in the ordered phase, a rich spectrum of two-kink bound states was observed (and even more structure was recently resolved by THz spectroscopy [4]) and understood in terms of confinement effects due to an effective longitudinal mean field resulting from the interchain couplings. Near the critical field, the ratios of the energies of the two lowest bound states approached the golden ratio, in agreement with long-standing, field-theory predictions for a universal E8 spectrum for the critical Ising chain perturbed by a weak longitudinal field [5].

In understanding the rich physics of $CoNb_2O_6$, the presence of the weak interchain couplings is essential, as they are responsible for the mean-field effects that lead to two-kink bound states via confinement effects in the ordered phase. Recent theoretical work [6] has highlighted potentially even richer physics due to the fact that the interchain couplings form a distorted (isosceles) triangular lattice with antiferromagnetic couplings. The resulting frustration effects, combined with the strong quantum fluctuations tuned by the transverse field, have been predicted to stabilize a fine structure inside the "ordered" part of the phase diagram. As many as four distinct ordered phases are predicted (including a zero-temperature incommensurate spin-density-wave state stabilized exclusively by quantum fluctuations) depending on the level of the isosceles distortion from the perfect (equilateral) triangular lattice. It is therefore of fundamental interest to obtain direct information about the geometry and strength of the interchain couplings and quantify the degree of the isosceles distortion of the triangular lattice.

The most direct measurement of the interchain couplings is via the dispersion of the excitations in the plane perpendicular to the magnetic chains. In the ordered phase where excitations are two-kink bound states, the interchain dispersion is much suppressed [7] and only occurs to higher order in the strength

of the interchain exchanges. The situation is very different in the quantum paramagnetic phase above the critical field, where the spontaneous order has disappeared. In this phase, the excitations can be understood as a first approximation by starting from the high-field limit, where they are coherently propagating single spin flips that can hop along all links of the lattice to first order in the corresponding exchange coupling strengths. Therefore, part of the motivation behind the experiments reported here is to probe with high-resolution inelastic neutron scattering the full 3D dispersion of the excitations in the quantum paramagnetic phase above the critical field and extract quantitatively the strength of the interchain couplings.

The phase above the critical field is described as a quantum paramagnet [1]. It is paramagnetic in the sense that the magnetization along the field is not yet saturated in the region immediately above the critical field (for the 1D Ising chain at the critical field, only about *half* the moment is polarized along the field [2]), such that there is a large part of the magnetic moment available that, in principle, could spontaneously order due to the Ising exchange. However, coherent quantum fluctuations induced by the transverse field suppress such order (as opposed to a thermal paramagnet at high temperature, where the spontaneous magnetic order is suppressed by random thermal fluctuations). The quantum paramagnet is smoothly connected (without any phase transition, only a crossover) to the fully polarized phase reached in the asymptotic limit of very high fields. The excitations in this whole region of the phase diagram can be understood by starting from the high-field limit, where they are coherently propagating single spin flips with a large (Zeeman) gap. Upon decreasing the field toward the critical field, quantum fluctuations increase and subsequently they decrease the magnetization along the field. At low energies, sharp, well-defined quasiparticles are expected throughout this phase, protected from decay because of the finite gap. However, the fundamental quantum nature of those quasiparticles is far from trivial. They originate from single spin flips, but are "dressed" by strong quantum fluctuations, and their dispersion relation may also be strongly renormalized compared to a semiclassical spin-wave description, which assumes that excitations are *literally* plane-wave superpositions of single spin flips. Therefore, another objective of the experiments reported here is to probe experimentally the full bandwidth of the dominant, along-chain dispersion in the quantum paramagnetic phase to see if the excitations are sharp over the full energy scale of the spectrum and test to what extent the dispersion can be quantitatively described by a spin-wave approach or whether quantum renormalization effects are relevant.

The crystal structure of $CoNb_2O_6$ is orthorhombic (space group $Pbcn$) and the magnetic ions are Co^{2+} occupying a single crystallographic site [8] [$4c(0,\zeta,1/4)$ with $\zeta = 0.165$] in a lattice of zigzag magnetic chains along the crystallographic c axis, with a triangular lattice arrangement in the basal ab plane, as illustrated in Fig. 1. Due to a combination of strong crystal-field and spin-orbit coupling effects, the magnetic ground state of the Co^{2+} ($3d^7$) ions is a Kramers doublet (effective spin $S = 1/2$) with a magnetic moment with a strong preference to point along a local easy axis (Ising direction z), located in the ac plane at a finite angle ($\gamma = 29.6^\circ$) to the c axis [8]. The magnetic interactions between neighboring

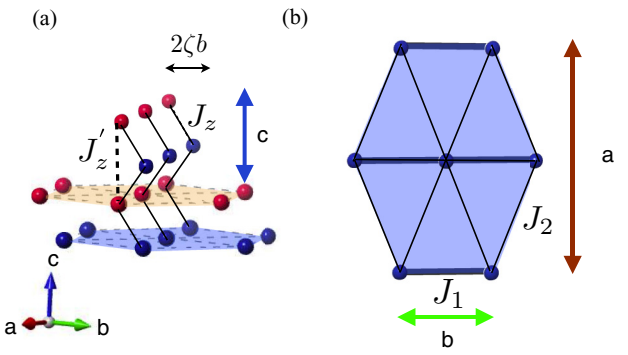

FIG. 1. (Color online) Lattice of Co^{2+} ions and relevant (Ising) exchange paths. (a) Zigzag chains running along c (and buckled along b) have a dominant ferromagnetic nearest-neighbor coupling J_z and weaker next-nearest-neighbor exchange J_z'. (b) The buckled magnetic chains form two inequivalent isosceles triangular lattices in the basal ab plane with interchain interactions J_1 (along the $\pm\boldsymbol{b}$ bonds) and J_2 [along the $(\pm\boldsymbol{a} \pm \boldsymbol{b})/2$ bonds]. For clarity, only the blue triangular lattice is shown.

Co^{2+} moments have been proposed to be of the Ising form $S_i^z S_j^z$, with the strongest interaction a ferromagnetic coupling J_z between nearest neighbors along the chain, followed by weaker antiferromagnetic (AFM) couplings J_z' between next nearest neighbors along the chain, and much weaker interchain couplings J_1 and J_2 along the bonds of the isosceles triangular lattice in the ab plane, both AFM [3,8]; see Fig. 1.

In zero applied magnetic field, the finite interchain couplings stabilize magnetic order below 2.95 K in a structure where spins are ordered ferromagnetically along the magnetic chains and the ordered spin magnitude varies between chains following an incommensurate wave vector $(0,q,0)$ with $q = 0.37$ just below the transition temperature [8,9]. Such an incommensurate spin-density-wave order is the natural ordering instability in an isosceles Ising triangular lattice, where at the onset temperature $q = \frac{1}{\pi}\cos^{-1}(\frac{J_2}{2J_1})$ (see Refs. [8,10]). The ordering wave vector was observed to be temperature-dependent upon cooling and to lock-in to the commensurate value $(0,1/2,0)$ at 1.97 K, below which the order is antiferromagnetic with a constant-magnitude ordered spin on every site. For magnetic fields applied along the b axis [3], transverse to the Ising axes, the spontaneous magnetic order is entirely suppressed at 5.5 T, and it is above this field that all measurements reported here have been collected.

The rest of the paper is organized as follows. Section II gives details of inelastic neutron scattering experiments performed to probe the magnetic excitations in the quantum paramagnetic phase in a high transverse field, and the results of those experiments are presented in Sec. III. The observed dispersion relations are parametrized first in Sec. IV A in terms of a phenomenological model of (spin-flip) quasiparticles that propagate by (spin-isotropic) hopping terms between the sites of the magnetic lattice. This captures well the low-energy modulations of the dispersion and the overall dispersion shape given the lattice topology of chains with a triangular lattice geometry in the basal plane. The model also accounts for the presence of an additional weaker intensity shadow mode, attributed to the magnetic unit cell doubling induced by

the buckling of the magnetic chains. This model, however, does not capture the observed suppression of the interchain dispersion at high energies. In Sec. IV B, we compare the magnetic excitations with predictions of a microscopic spin exchange Hamiltonian with dominant Ising coupling along the chain direction and additional further neighbor exchanges solved in the linear spin-wave approximation. We first present a one-sublattice approximation in Sec. IV B 1 and then a four-sublattice model appropriate for the orthorhombic crystal structure in Sec. IV B 2. We show that the latter can provide a very good parametrization of the observed dispersions, intensity dependence in the Brillouin zone, and relative intensity between the main and shadow modes. In Sec. V, we discuss the fact that the observed dispersion bandwidth is smaller than the calculated bandwidth using a linear spin-wave approach using exchange values estimated earlier from a parametrization of the spin dynamics in zero applied field. We propose that the observed smaller dispersion bandwidth is due to a quantum renormalization of the dispersion at fields not too high above the critical transverse field not captured by spin-wave theory. We discuss this effect in detail for the pure Ising chain in a transverse field by comparing the known exact quantum solution with linear spin-wave results. Finally, conclusions are summarized in Sec. VI.

II. EXPERIMENTAL DETAILS

A 7 g single crystal of $CoNb_2O_6$ grown using the floating zone technique [11] was mechanically fixed inside a custom-made oxygen-free copper can to prevent sample movement due to strong torques that arise when an external magnetic field is applied transverse to the Ising axis of the spins at low temperatures. The crystal was aligned in the horizontal $(h0l)$ plane, which contains both the c direction of the magnetic chains and the Ising direction. Throughout this paper, wave-vector components (h,k,l) are given with reference to the reciprocal lattice of the crystallographic orthorhombic unit cell with lattice parameters $a = 14.1337$ Å, $b = 5.7019$ Å, and $c = 5.0382$ Å at 2.5 K from Ref. [8]. The sample mount was attached to the bottom of a dilution refrigerator insert with a base temperature of 0.03 K. Magnetic fields were applied along the b axis (transverse to the Ising axes of all spins) using a vertical superconducting magnet. All measurements reported here were made in fields between 7 and 9 T in the quantum paramagnetic phase above the quantum critical phase transition at 5.5 T.

Inelastic neutron scattering experiments were performed using both the multiangle triple-axis MACS [12] spectrometer at the NIST Center for Neutron Research as well as the direct-geometry time-of-flight chopper spectrometer LET [13] at ISIS. MACS was operated to measure the inelastic scattering of neutrons with a fixed final energy $E_f = 3$ meV as a function of wave-vector transfer in the horizontal $(h0l)$ scattering plane at constant energy transfer (from $E = 0.4$ to 2.75 meV). This enabled probing the magnetic excitations along the chain direction l, as well as along the interchain direction h, with typical counting times of 2 h to collect a complete wave-vector map at a fixed energy transfer.

On LET, the inelastic scattering was probed for neutrons with incident energies of $E_i = 2.1$, 4, and 10 meV with a measured energy resolution [full width at half-maximum (FWHM)] on the elastic line of 0.023(1), 0.051(1), and 0.21(1) meV, respectively. LET was operated to record the time-of-flight data for incident neutron pulses of all the above different energies simultaneously. The large vertical opening of the magnet on LET allowed probing the inelastic scattering using position-sensitive detectors along the direction perpendicular to the scattering plane, i.e., the k direction, which was essential in order to obtain a complete map of the dispersions in the full 3D Brillouin zone. The inelastic scattering was measured for a selection of fixed sample orientations to probe the full bandwidth of the magnetic dispersion along the chain direction l and also along the interchain h and k directions near the along-chain ferromagnetic zone center $l = 0$, with typical counting times of 2 h per fixed sample orientation setting. Furthermore, a series of measurements at fixed sample orientations spanning an angular range of 90° in 1° steps (counting time 3 min/step) were combined into a Horace [14] four-dimensional volume file to extract the complete magnetic dispersion maps in the $(hk0)$ plane perpendicular to the magnetic chains. All data sets were collected at fixed temperatures between 0.03 and 1.8 K. Even the highest temperature satisfied the criterion that it was much smaller than the spin gap (0.389 meV at 7 T), so thermal effects to the measured dispersions are expected to be negligible.

III. MEASUREMENTS AND RESULTS

A. Dispersion along the chain direction

The observed inelastic neutron scattering spectrum at 9 T shown in Fig. 2(a) is dominated by a single mode with a small linewidth at low energies and over most of the dispersion bandwidth. The largest dispersion bandwidth is along the chain direction (2.85 meV) with a near-sinusoidal shape with the minimum (0.92 meV) at the zone center $l = 0$ and periodicity $l \rightarrow l + 2$, as expected for dominant ferromagnetic coupling between spins spaced by $c/2$ along the chain direction; see Fig. 1(a). For finite interchain wave-vector component k, a much weaker intensity "shadow" mode is also observed with the same dispersion relation as the main mode, but shifted by

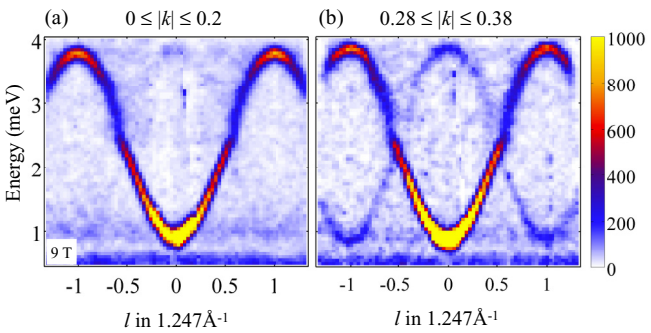

FIG. 2. (Color online) Dispersion along the chain direction l in the paramagnetic phase at 9 T and ~0.03 K, measured on LET with an incident energy $E_i = 10$ meV. (a) A single dispersive mode is observed for small interchain wave-vector component k, and (b) a second, weaker-intensity mode becomes visible for finite k. The plots show the averaged neutron scattering intensity for $|k|$ in the range [0.0,0.2] in (a) and [0.28,0.38] in (b).

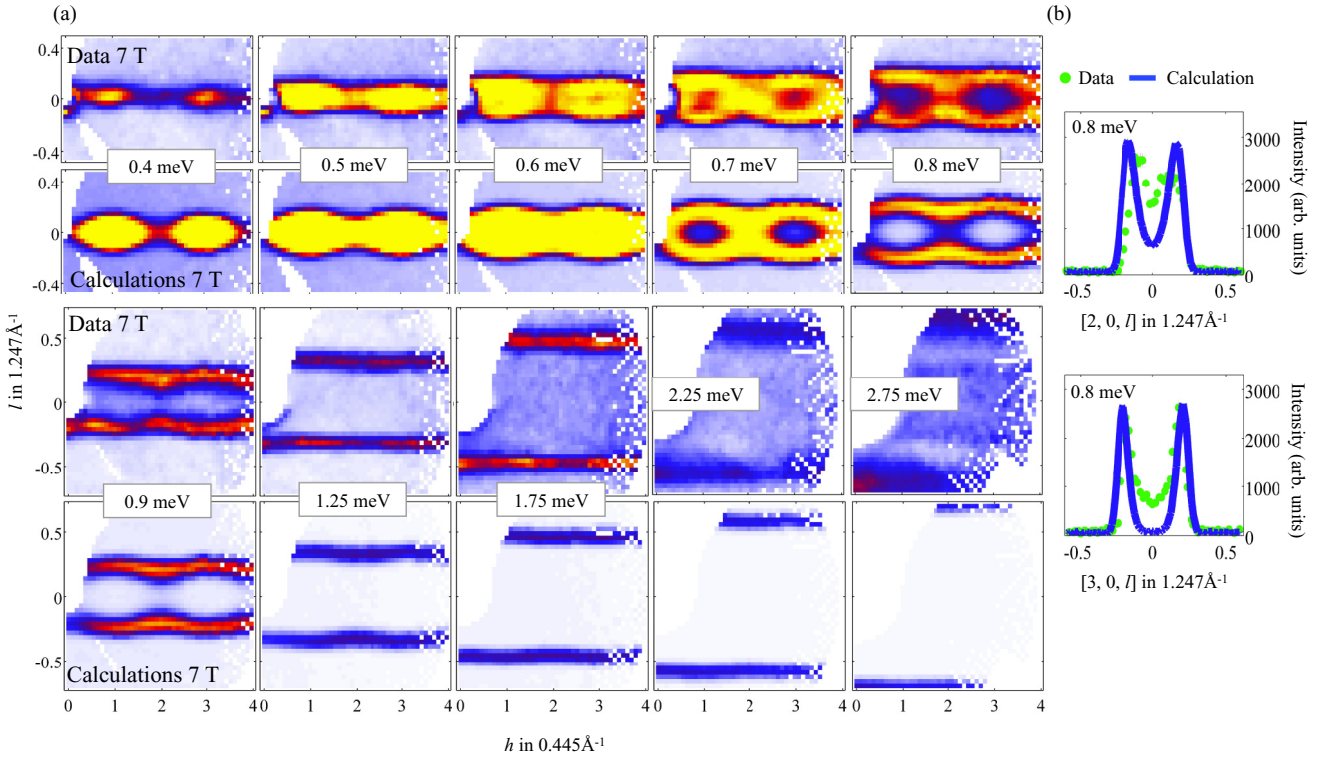

FIG. 3. (Color online) (a) Inelastic neutron scattering intensity at constant energy transfer E as a function of wave vector in the $(h0l)$ plane measured at 7 T and 0.5 K on MACS. Rows 1 and 3 are data, rows 2 and 4 are calculations using the one-sublattice spin-wave model in Eq. (3) with intensities given in Eq. (6) and an overall single intensity scaling factor for all the panels. The calculations include the neutron polarization factor, the spherical magnetic form factor for Co^{2+}, and instrumental resolution effects. At low energies, near the dispersion minimum, strong dispersion is seen along both h and l. As the energy increases, the dispersion along the interchain direction h becomes flatter, suggesting that interchain couplings become less relevant at higher energies. (b) Wave-vector scans along (2,0,l) and (3,0,l) at constant energy transfer $E = 0.8$ meV showing displacement of the spin-wave peaks upon changing h, data (green circles) and spin-wave model (blue line). Error bars represent ± 1 standard deviation.

$l \rightarrow l + 1$; see Fig. 2(b). As we will show later, this is due to the fact that the magnetic chains are not straight but buckled [see Fig. 1(a)], and this buckling leads to an effective doubling of the magnetic unit cell along c (compared to straight chains) and zone folding leads to the observed shadow mode.

B. Interchain dispersion

To probe the sensitivity of the dispersion relations to the interchain couplings, detailed measurements of the inelastic spectrum were first performed in the $(h0l)$ plane at a somewhat lower field of 7 T (still in the quantum paramagnetic phase) and are shown in Fig. 3. Constant energy maps of the inelastic neutron scattering are plotted along the interchain direction h (horizontally) and along the chain direction l (vertically) for energy transfers E starting from the minimum of the dispersion near 0.4 meV and up to 2.75 meV. Compared to the 9 T data in Fig. 2(a) at this lower field of 7 T, the spin gap is reduced due to the decrease in Zeeman energy. The regions of strong intensity indicate the location of the constant energy contours in the dispersion surface. For decoupled magnetic chains along c, the dispersion would be expected to depend only on l and be independent of h, so constant energy contours would be expected to be parallel horizontal lines that move further apart in l with increasing energy. The data, however, show very clear modulations of the constant energy contours along both h and l, in particular at the lower energies toward the minimum gap. For example, a dispersion along h is very clearly seen at $E = 0.8$ meV in Fig. 3(a) (top right panel) and it is also very pronounced at the lowest energies $E = 0.4$ meV (top left panel) where minima in the shape of rugby balls are centered at odd h positions. The data indicate that interchain couplings produce important modulations in the dispersion relation at low energies near the minimum gap with weaker effects (less interchain dispersion) at higher energies above $\sim$1.25 meV.

Higher-resolution measurements of the dispersion relations at this same field (7 T) illustrating the full bandwidth along the chain direction and along two orthogonal interchain directions are shown in Figs. 4(a)–4(d). The dispersion bandwidth in the $(hk0)$ plane is much smaller than the along-chain dispersion, as expected for weakly coupled chains [0.16 and 0.05 meV along $(h00)$ and $(1k0)$, respectively, above a gap of 0.39 meV, compared to 2.7 meV along l]. The inelastic neutron scattering intensity as a function of wave vector in the $(hk0)$ plane is plotted for different energies in the panels of Fig. 5(a), where black lines denote the Brillouin zone boundaries of the triangular lattice in the ab plane. The regions of strong scattering follow a dispersion resembling the Fourier transform of a triangular lattice with antiferromagnetic couplings showing a maximum energy near the zone centers (000) and (200) (visible in the

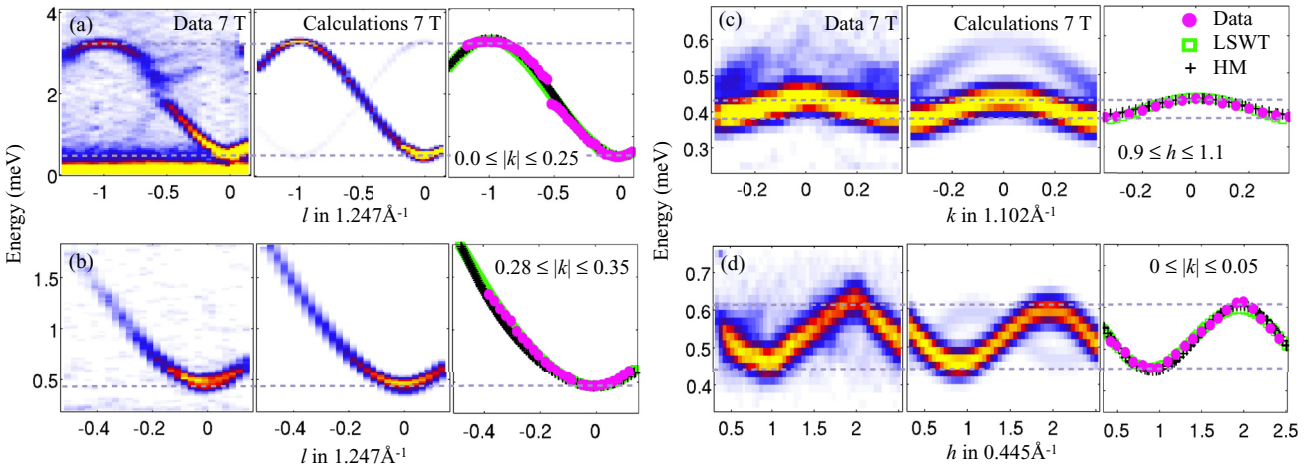

FIG. 4. (Color online) Inelastic neutron scattering intensity as a function of wave vector and energy transfer measured on LET at 7 T and ∼0.06 K (left), calculated intensity using the four-sublattice spin-wave model (center) described in Sec. IV B 2 and comparison between dispersion data points (magenta filled circles) with the spin-wave dispersion relation Eq. (3) (LSWT, green square) and the hopping model Eq. (1) (HM, black cross) (right). Horizontal gray dashed lines are guides to the eye to emphasize the bandwidth of the dispersion along various directions. The calculated intensities include the neutron polarization factor, the spherical magnetic form factor for Co^{2+}, and instrumental resolution effects. (a) Dispersion along the chain direction l showing the full bandwidth of 2.7 meV ($E_i = 10$ meV). (b) Zoom into the low-energy part of the dispersion along l showing the energy gap at 0.48 meV ($E_i = 4$ meV). (c) Dispersion along the interchain direction k for wave vectors near $(1,k,0)$ with a bandwidth of 0.05 meV. Note in the data (left panel) the presence at large $|k|$ and energies above the main mode of additional scattering intensity that decreases rapidly as $k \to 0$. This is attributed (middle panel) to the shadow mode that appears because of the unit cell doubling in the ab plane due to the alternate rotation of Ising axes. (d) Dispersion along the interchain direction h for wave vectors near $(h,0.025,0)$ showing minima at odd h and a bandwidth of 0.16 meV.

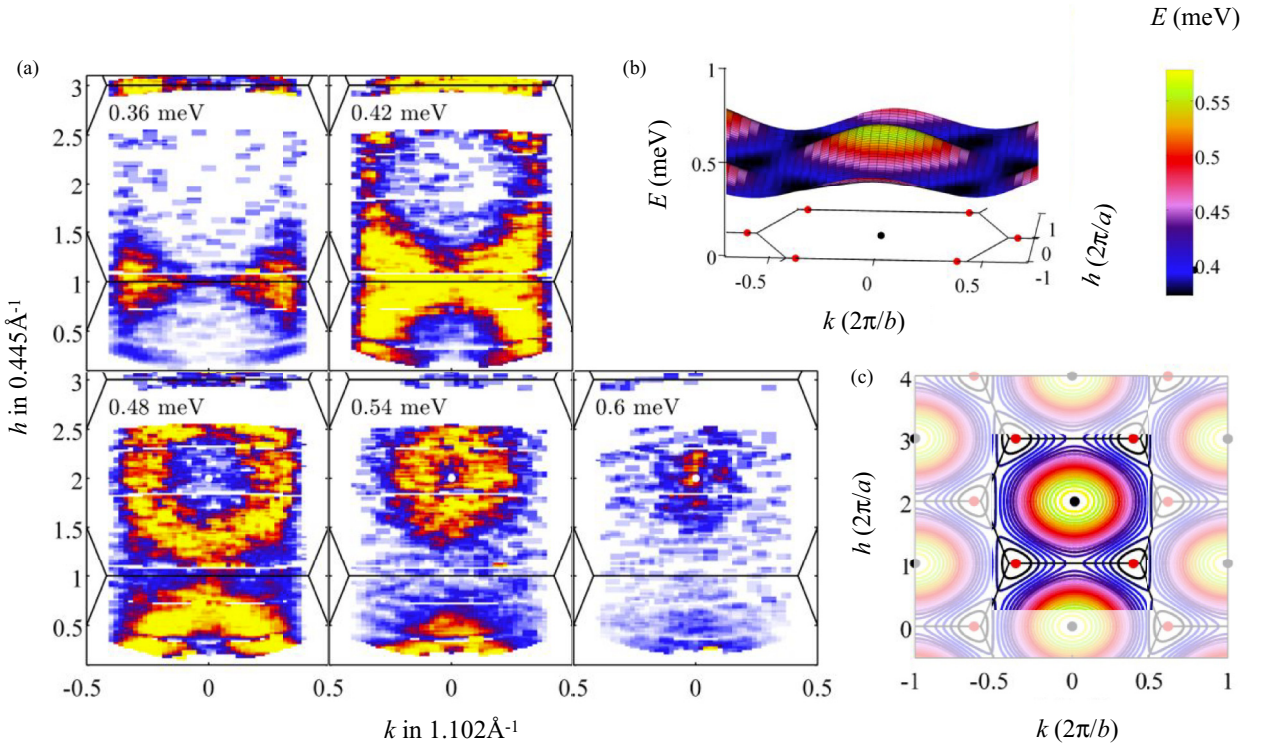

FIG. 5. (Color online) (a) Observed neutron scattering intensity in constant energy slices as a function of wave vector in the $(hk0)$ plane at 7 T and 1.8 K, extracted from a four-dimensional Horace scan on LET. Regions of strong intensity show the constant-energy contours of the interchain dispersion in the triangular ab plane. Each slice shows data averaged for energies within ±0.03 meV of the nominal value. Solid lines show the edges of the hexagonal Brillouin zone of the triangular lattice. (b) Surface plot of the interchain dispersion using Eqs. (3)–(8) and (c) projection contour plot in the $(hk0)$ plane. Solid black circles show the Brillouin zone centers (nuclear Bragg peak positions) of the triangular lattice, and solid red circles indicate minimum gap positions of the dispersion surface. In (c) the highlighted area shows the momentum space probed experimentally in (a).

bottom right panel $E = 0.6$ meV) and minimum energy near $(1,\pm q,0)$ with $q \sim 1/3$ (top-left panel $E = 0.36$ meV).

IV. ANALYSIS

From the multidimensional inelastic neutron scattering data, dispersion points were extracted by fitting Gaussian peaks to scans in energy or wave vector to obtain the full wave vector (h,k,l) and energy position E of the intersection of each scan direction with the dispersion surface. Since the LET data provided high-resolution measurements of the dispersion relations along all three directions in reciprocal space, dispersion points (h,k,l,E) extracted from fitting datasets such as those shown in magenta dots in Figs. 4(a)–4(d) (right panels) were then used for the quantitative fits from the models to be discussed below. The obtained parametrization was checked for consistency against the MACS data for wave vectors in the $(h0l)$ plane.

A. Spin-flip hopping model

To parametrize the observed dispersions, we first consider a phenomenological model of spin-flip excitations that propagate by hopping between lattice sites, where the dispersion is the Fourier transform of the hopping terms. We assume a magnetic lattice of straight chains along c ($\zeta = 0$) coupled in a triangular arrangement in the basal plane. The dispersion relation for nearest-neighbor hops is

$$\hbar\omega_{\boldsymbol{k}} = E_0 + 2t_0\cos\pi l + 2t_1\cos 2\pi k + 4t_2\cos\pi k\cos\pi h. \tag{1}$$

Here E_0 is the average energy (midpoint of the dispersion band), and t_0, t_1, and t_2 describe the hoppings along the bonds $\pm\boldsymbol{c}/2$ (J_z bond), $\pm\boldsymbol{b}$ (J_1 bond), and $\pm\frac{\boldsymbol{a}}{2} \pm \frac{\boldsymbol{b}}{2}$ (J_2 bond), respectively, as illustrated in Fig. 1. The spin-flip hopping between sites physically originates from spin exchange on the corresponding bonds with the hopping energy t encoding the strength (and sign) of the spin interaction ($t > 0$ for antiferromagnetic coupling). In the case of all bonds having spin-isotropic exchanges of the type $J\boldsymbol{S}_i \cdot \boldsymbol{S}_j$, the magnetic excitations in the fully polarized phase at high applied field are indeed single spin flips with hopping $t = SJ$; for anisotropic exchanges and transverse fields, the dispersion is expected to have a sinusoidal form as in Eq. (1) only in the perturbative limit of small exchanges compared to the Zeeman energy [1].

We find that at high field (7 T) the overall shape and low-energy modulations in the dispersion relation of the main mode can be well described by the nearest-neighbor hopping model in Eq. (1) [see Fig. 4 (right panels, magenta filled circles are the data points and black crosses denote the model)] with fitted parameter values

$$E_0 = 1.857(3)\text{ meV}, \quad 2t_0 = -1.402(2)\text{meV},$$
$$t_2/t_1 = 0.82(1), \quad 2t_1 = 0.0511(7)\text{meV}.$$

The model can reproduce the dispersion relation along the chain direction ($t_0 < 0$ means ferromagnetic exchange along the chain) [see Fig. 4(a) (right panel)] as well as the dispersions in the interchain $(hk0)$ plane, which is that of a triangular lattice with antiferromagnetic nearest-neighbor couplings ($t_{1,2} > 0$) [see Figs. 4(c) and 4(d) (right panels)]. The fitted hopping parameters give $t_2/t_1 < 1$ as expected for an isosceles triangular lattice.

1. *Shadow mode due to buckling of chains*

The presence of the additional weaker intensity shadow mode in Fig. 2(b) for finite k can also be explained within a hopping model by including the buckling of the magnetic chains, see Fig. 1(a), where consecutive ions along the chain are alternatingly displaced by $\pm\zeta\boldsymbol{b}$. This buckling along b leads to a doubling of the magnetic unit cell along c (compared to straight chains), and zone folding of the main mode dispersion, Eq. (1), leads to the appearance of a second mode with the same dispersion relation, but shifted in wave vector by $l \to l + 1$, as observed in Fig. 2(b). Using a spin-flip hopping model on the corresponding two-sublattice problem, we obtain the intensity of the two modes in inelastic neutron scattering as $I_{\boldsymbol{k}}^{\pm} = A^{\pm}[1 \pm \cos(4\pi\zeta k)]$, with the upper (lower) sign for the main (shadow) mode. This predicts that the main mode is strongest and the shadow mode absent at $k = 0$, with the shadow mode intensity increasing quadratically as $|k|$ increases from 0, which is consistent with the observation of the shadow mode only at finite k in Figs. 2(a) and 2(b). Quantitatively, the experimentally observed k dependence of the intensity of the two modes extracted from the data shown in Fig. 2 is well described by the above functional forms as shown in Fig. 6 [data, open and filled circles; fits, solid and dashed lines].

We note, however, that the ratio of the extracted intensity prefactors of the shadow and main mode, $A^-/A^+ = 2.5(2)$ at $l = -1$, cannot be accounted for within the hopping model, which predicts $A^- = A^+$, both constants, independent of wave vector. The hopping model predicts constant intensity for the dispersion along l (as expected for isotropic spin exchanges), whereas the data clearly show intensity decreasing upon increasing energy and wave vector away from $l = 0$ [see Fig. 4(b) (left panel)]. This intensity modulation with a maximum near $l = 0$ (gap minimum) is phenomenologically understood as an increase in scattering weight at low energies in anticipation of the critical phase transition at lower field near 5.5 T.

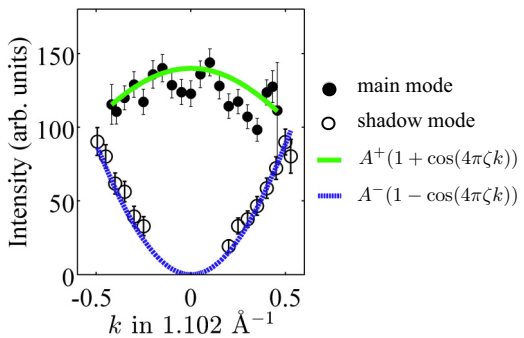

FIG. 6. (Color online) Intensity of the main (shadow) mode [filled (open) circles] as a function of the interchain wave vector k, fitted to the functional form for a buckled magnetic chain [green solid (blue dashed) line], as described in the text. The intensities were extracted at the ferromagnetic zone boundary $l = -1$ from the same data set as in Fig. 2. Error bars represent ± 1 standard deviation.

Another shortcoming of the hopping model is that although it accounts well for the observed modulations in the interchain dispersion at the lowest energies near $l = 0$, it predicts the same magnitude interchain dispersion also at higher energies, whereas experimentally it is observed that the dispersion relation becomes more one-dimensional (less interchain dispersion) at higher energies, as shown in Fig. 3, where constant energy contours are strongly modulated along both h and l at low energies, but they become almost independent of h at high energies above ∼1.25 meV. Those shortcomings of the hopping model in describing the intensity maximum near the gap minimum and suppression of the interchain dispersion at higher energies are better accounted for by including anisotropic spin exchange interactions, as described in the following section.

B. Linear spin-wave model

To better account for the observed dispersion and intensity modulations in the 3D Brillouin zone, we parametrize the data in terms of a microscopic spin Hamiltonian with anisotropic spin exchanges.

1. One-sublattice spin-wave model

We start with straight chains along c ($\zeta = 0$) with a dominant nearest-neighbor ferromagnetic Ising exchange J_z (see Fig. 1) between the S^z spin components and a smaller exchange J_{xy} between the S^x and S^y spin components. As subleading terms, we include an Ising second neighbor exchange J_z' along the chains for the $\pm\boldsymbol{c}$ bonds, and Ising interchain couplings J_1 and J_2 along the $\pm\boldsymbol{b}$ and $\pm\frac{\boldsymbol{a}}{2} \pm \frac{\boldsymbol{b}}{2}$ bonds, respectively [15]. To start with, we also assume that the local Ising axes (z) are the same for all sites [along the c axis ($\gamma = 0$)]. This ensures that we deal with a one-sublattice magnetic unit cell of basis vectors $(\boldsymbol{a} - \boldsymbol{b})/2$, $\boldsymbol{b}$, and $\boldsymbol{c}/2$. Including also a magnetic field applied along x (transverse to the Ising axis z), the Hamiltonian reads

$$\begin{aligned}\mathcal{H} = \sum_{\boldsymbol{r}} & -J_z S^z_{\boldsymbol{r}} S^z_{\boldsymbol{r}+\boldsymbol{c}/2} - J_{xy}\left[S^x_{\boldsymbol{r}} S^x_{\boldsymbol{r}+\boldsymbol{c}/2} + S^y_{\boldsymbol{r}} S^y_{\boldsymbol{r}+\boldsymbol{c}/2}\right] \\ & + J_z' S^z_{\boldsymbol{r}} S^z_{\boldsymbol{r}+\boldsymbol{c}} + J_1 S^z_{\boldsymbol{r}} S^z_{\boldsymbol{r}+\boldsymbol{b}} + J_2 S^z_{\boldsymbol{r}} S^z_{\boldsymbol{r}+(\boldsymbol{a}+\boldsymbol{b})/2} \\ & + J_2 S^z_{\boldsymbol{r}} S^z_{\boldsymbol{r}+(\boldsymbol{a}-\boldsymbol{b})/2} - g\mu_B B S^x_{\boldsymbol{r}}, \end{aligned} \tag{2}$$

where $g\mu_B B$ is the Zeeman energy, $S = 1/2$, and $\boldsymbol{r}$ runs over all magnetic lattice sites. We find that J_z and J_{xy} are ferromagnetic, whereas J_z', J_1, and J_2 are antiferromagnetic. The dispersion relations of the above Hamiltonian are exactly solvable only in some special cases, such as when $J_{xy} = J_z' = J_1 = J_2 = 0$, i.e., decoupled Ising chains in a transverse field [2], and some related models [16]. In the asymptotic limit of very high fields when spins are nearly ferromagnetically polarized along the applied field direction, the excitations can be described using linear spin-wave theory. Our experiments were performed at applied fields not high enough to be in this limit, but in the absence of an alternative quantitative theory that could include all exchanges, we have used linear spin-wave theory to parametrize the excitations with the expectation that the fitted exchange values might be renormalized from their actual values.

Assuming a mean-field fully polarized ground state, the spin-wave dispersion relation of the Hamiltonian in Eq. (2) is obtained as

$$\hbar\omega_{\boldsymbol{k}} = \sqrt{A_{\boldsymbol{k}}^2 - B_{\boldsymbol{k}}^2}, \tag{3}$$

where

$$\begin{aligned} A_{\boldsymbol{k}} &= g\mu_B B - S[J_z(\boldsymbol{k}) + J_{xy}(\boldsymbol{k})] + 2SJ_{xy}(\boldsymbol{0}), \\ B_{\boldsymbol{k}} &= -S[J_z(\boldsymbol{k}) - J_{xy}(\boldsymbol{k})], \end{aligned} \tag{4}$$

and where the Fourier-transformed exchanges are

$$\begin{aligned} J_z(\boldsymbol{k}) =& J_z \cos\pi l - J_z' \cos 2\pi l - J_1 \cos 2\pi k \\ & - 2J_2 \cos\pi k \cos\pi h, \\ J_{xy}(\boldsymbol{k}) =& J_{xy} \cos\pi l. \end{aligned} \tag{5}$$

The intensity in neutron scattering is proportional to the dynamical correlations obtained (see Appendix) as $S^{zz}(\boldsymbol{k}, E) = \frac{S}{2}\frac{A_{\boldsymbol{k}} - B_{\boldsymbol{k}}}{\hbar\omega_{\boldsymbol{k}}}\delta(E - \hbar\omega_{\boldsymbol{k}})$ for the fluctuations polarized along the Ising axis z, and $S^{yy}(\boldsymbol{k}, E) = \frac{S}{2}\frac{A_{\boldsymbol{k}} + B_{\boldsymbol{k}}}{\hbar\omega_{\boldsymbol{k}}}\delta(E - \hbar\omega_{\boldsymbol{k}})$ for the fluctuations along y, the axis perpendicular to the plane defined by the Ising axis and the applied field. Here δ is the Dirac delta function. For direct comparison with the experiment, the expected neutron scattering intensity including polarization factors is given by

$$I(\boldsymbol{k}, E) = \left(1 - \frac{\kappa_y^2}{\kappa^2}\right) S^{yy}(\boldsymbol{k}, E) + \left(1 - \frac{\kappa_z^2}{\kappa^2}\right) S^{zz}(\boldsymbol{k}, E), \tag{6}$$

where

$$\kappa_y = 2\pi h/a, \quad \kappa_z = 2\pi l/c, \quad \kappa = \sqrt{\kappa_y^2 + \kappa_z^2}. \tag{7}$$

The strongest intensity is predicted for fluctuations polarized along the Ising axis z at low energies near the 3D dispersion minima points at (odd, q, 0) and (even, $1 - q$, 0) with $q = \frac{1}{\pi}\cos^{-1}(\frac{J_2}{2J_1})$. A contour plot of the dispersion surface in the $(hk0)$ plane is shown in Fig. 5(c).

2. Four-sublattice spin-wave model

The one-sublattice spin Hamiltonian in Eq. (2) can be readily extended to the full generality of the actual crystal structure, where the magnetic chains along c are not straight but buckled [see Fig. 1(a)], and the local Ising axes are not the same for all sites but alternate in orientation between $\hat{\boldsymbol{z}}, \hat{\boldsymbol{z}}' = \pm\sin\gamma\,\hat{\boldsymbol{a}} + \cos\gamma\,\hat{\boldsymbol{c}}$ for magnetic chains translated by $(\pm\boldsymbol{a} \pm \boldsymbol{b})/2$. For example, if we were to identify the local Ising axes in Fig. 1(b), even and odd b-axis "rows" of spins would show that the local Ising axes alternate between $\hat{\boldsymbol{z}}$ and $\hat{\boldsymbol{z}}'$. Here $\hat{\boldsymbol{a}}$ and $\hat{\boldsymbol{c}}$ are unit vectors along the orthorhombic a and c axes, respectively. To compare the results directly with the one-sublattice model, we will assume that the interchain exchanges still couple only the local Ising spin components on the different chains, i.e., $J_1 S^z_{\boldsymbol{r}} S^{z'}_{\boldsymbol{r}+\boldsymbol{b}}$ and $J_2 S^z_{\boldsymbol{r}} S^{z'}_{\boldsymbol{r}+(\boldsymbol{a}\pm\boldsymbol{b})/2}$.

By solving this four-sublattice model (the magnetic unit cell equals the structural, orthorhombic unit cell) via numerical diagonalization of the quadratic spin-wave Hamiltonian, we obtained four dispersive modes: one mode has the same dispersion, Eq. (3), as the one-sublattice problem in Eq. (2), and the other three modes are obtained by a shift in wave

vector. This can be intuitively understood starting from the one-sublattice problem: the buckling of the chains and nonequivalence of Ising axes between chains translated by $(\pm\boldsymbol{a} \pm \boldsymbol{b})/2$ leads to a doubling of the magnetic unit cell along c and also a doubling in the ab plane. New magnetic zone centers appear at positions such as (001) and (100), and consequently new dispersion modes appear, which are images of the main mode shifted in wave vector to the new zone-center positions. In total, three additional shadow modes appear with dispersion relations $\hbar\omega_{(h,k,l+1)}$ [as seen in Fig. 2(b)], $\hbar\omega_{(h+1,k,l)}$ [as seen in Fig. 4(c) (left and middle panels)], and $\hbar\omega_{(h+1,k,l+1)}$.

The experimentally observed dispersion relation of the main mode can be well-described by the spin-wave model in Eq. (3), when all exchange values are included and have finite values (attempts to fit the dispersion to a restricted set of parameters, such as fixing $J_{xy} = 0$ or $J_z' = 0$, did not provide good fits). However, the dispersion data alone are not sufficiently constraining to independently determine the absolute values of all five exchanges and the Zeeman term because changes in parameter values produce changes to the dispersion that are strongly coupled to one another. In particular, the effects of J_z and J_{xy} are to vary the dispersion bandwidth by affecting both the minimum and maximum energies; the B-field overall shifts the dispersion to higher energies, but it also affects slightly the dispersion bandwidth; J_z' overall shifts the dispersion and produces a modulation with periodicity $l \rightarrow l + 1$. Even the dispersion bandwidth in the plane normal to the chains depends not only on the strength of the interchain couplings $J_{1,2}$, but also the Zeeman term $g\mu_B B$, as can be explicitly seen by inspecting the form of the dispersion relation at $l = 0$,

$$\hbar\omega_{(h,k,0)} = \sqrt{C + 2g\mu_B BS[J_1 \cos 2\pi k + 2J_2 \cos \pi k \cos \pi h]},$$

where $C = g\mu_B B[g\mu_B B - 2S(J_z - J_z' - J_{xy})]$. Note that the prefactor in front of the Fourier transform of the interchain terms is not a constant, but depends on the Zeeman term. So effectively the absolute values of *all* exchange parameters and the Zeeman term are strongly coupled to one another within the spin-wave dispersion form, and as a consequence several sets of parameter values can give rather similar agreement with the observed dispersions, as we indeed find. The only parameter that is relatively constrained by the parametrizations (and for which we can provide a meaningful uncertainty) is the interchain frustration ratio J_2/J_1. To illustrate the level of agreement that can be obtained, we list below *representative* values for the parameters that give one of the lowest χ^2 values in terms of a comparison with the dispersions at 7 T,

$$\begin{aligned} J_z &= 2.19 \text{ meV}, \quad g\mu_B B = 1.66 \text{ meV}, \\ J_{xy} &= 0.36 \text{ meV}, \quad J_z' = 0.29 \text{ meV}, \\ J_1 &= 0.031 \text{ meV}, \quad J_2/J_1 = 0.77(10) \text{ meV}, \end{aligned} \tag{8}$$

and at 9 T,

$$\begin{aligned} J_z &= 2.4 \text{ meV}, \quad g\mu_B B = 2.0 \text{ meV}, \\ J_{xy} &= 0.4 \text{ meV}, \quad J_z' = 0.36 \text{ meV}, \\ J_1 &= 0.036 \text{ meV}, \quad J_2/J_1 = 0.75(10) \text{ meV}. \end{aligned} \tag{9}$$

These parametrizations capture well all key modulations of the observed dispersions. They also reproduce well the overall intensity dependence (using the four-sublattice model), as illustrated in Figs. 3, 4, and 5. Furthermore, they reproduce quantitatively the observed relative intensity ratio between the main and shadow modes in Fig. 6, and they capture the fact that the observed interchain dispersion is largest at the lowest energies near $l = 0$ and becomes progressively less pronounced at higher energies.

We note that in all parametrizations, the ratio of the interchain exchange couplings is consistent with the expectation of an isosceles triangular lattice ($J_2/J_1 < 1$). This would give an instability to magnetic order at an incommensurate wave vector $q = \frac{1}{\pi}\cos^{-1}(\frac{J_2}{2J_1}) \sim 0.37(2)$, consistent with the value observed experimentally at the onset of magnetic order, q ($T_N = 2.95$ K) $= 0.37$ (see Ref. [8]), further supporting the idea that frustrated interchain couplings stabilize the incommensurate spin-density-wave magnetic order observed at zero field just below T_N.

For completeness, we note that an unexpected feature in the data, not captured by the spin-wave model, is an apparent broadening of the magnetic scattering intensity and a departure of the local dispersion slope away from the model predictions in a finite energy range just above the midpoint of the dispersion bandwidth along the chain direction; see the 7 T data in Fig. 4(a) (left panel) in the approximate energy range 1.8–2.3 meV. Similar anomalies are also observed upon close inspection in the 9 T data in Fig. 2(a) in a finite energy range (2.4–3 meV), again just above the midpoint of the dispersion bandwidth. Those anomalous broadening effects at intermediate energies will be addressed in detail elsewhere [17].

V. DISCUSSION

We now compare the parametrization of the dispersions with previous estimates of the exchange couplings obtained from analyzing the excitations in zero field [3], where the spectrum consisted of a series of sharp modes strongly dispersing along the chain direction and attributed to bound states of pairs of domain walls (kinks) on the magnetic chains. This spectrum was well explained by an effective Hamiltonian for kinks [3,18], which contained the energy cost J required to create two kinks in the absence of other perturbations, a kink hopping term, α, tuning the dispersion bandwidth, and terms β and β' to account for the energy of a kinetic bound state stabilized near the ferromagnetic zone boundary ($l = -1$). In addition, a longitudinal effective field h_z was assumed responsible for the confinement of pairs of kinks into bound states. Mapping the spin Hamiltonian (2) at zero external field ($B = 0$) into an effective Hamiltonian for kinks in the limit of small perturbations from the Ising limit (J_z dominant) reproduces several terms in the phenomenological kink Hamiltonian in Ref. [3]. These terms are $J = J_z - 2J_z'$, $\beta = J_{xy}/2$, $\beta' = J_z'$, and the mean field due to 3D long-range order in the antiferromagnetic pattern with $q_{AF} = (0,1/2,0)$ is $h_z = 2J_1\langle S^z\rangle$, where $\langle S^z\rangle$ is the expectation value of the ordered spin moment. The kink hopping term α is not captured in this mapping; it must originate microscopically from a magnetic interaction term not considered in Eq. (2). Using the zero-field values for J, β, and β' from Ref. [3] gives $J_z = 2.76$ meV, $J_{xy} = 0.66$ meV, and $J_z' = 0.41$ meV. We note that a more elaborate analysis of the zero-field excitation spectrum

(using numerical matrix-product state methods for 1D chains expected to be accurate even in the presence of substantial perturbations away from the Ising limit) proposed somewhat similar values [16], $J_z = 2.43$ meV, $J_{xy} = 0.52$ meV, and $J_z' = 0.60$ meV. The observed dispersion at 7 and 9 T cannot be quantitatively described by either of the above two sets of exchanges by only allowing as free parameters the Zeeman energy and the interchain couplings J_1 and J_2; the observed dispersion bandwidth along the chain direction is systematically smaller than the prediction. We attribute this effect to a quantum renormalization on the dispersion relation in the quantum paramagnetic phase beyond the linear spin-wave approximation, as explained below.

A. Quantum renormalization effects on the spin-wave dispersion

To appreciate why spin-wave theory does not capture quantitatively the dispersion relation in the quantum paramagnetic phase, it is insightful to consider the pure 1D Ising chain in transverse field, i.e.,

$$\mathcal{H} = \sum_i -J_z S_i^z S_{i+1}^z - h S_i^x, \tag{10}$$

where i indexes consecutive sites along the chain, J_z is the ferromagnetic Ising coupling, h is the transverse field, and $S = 1/2$. The semiclassical mean-field approach predicts suppression of the spontaneous ferromagnetic Ising order at the classical critical field $h_c^{\rm cl} = J_z$ with the spin-flip dispersion at higher field,

$$\hbar\omega^{\rm cl} = \sqrt{h^2 - hJ_z \cos \pi l} \tag{11}$$

(for spacing $c/2$ along the chain). In contrast, the exact quantum solution (obtained via mapping to Jordan-Wigner fermions [1,2]) gives the critical field at *half the classical value*, i.e., $h_c = J_z/2$, with the quasiparticle dispersion at higher field,

$$\hbar\omega = \sqrt{h^2 - hJ_z \cos \pi l + \frac{J_z^2}{4}}. \tag{12}$$

Both the classical and quantum dispersions tend to the same form, $h - \frac{J_z}{2} \cos \pi l$, in the perturbative limit near very high field $h/J_z \to \infty$, but there are very significant differences at fields comparable to the exchange strength. The strong renormalization of the critical field means that for fields in the range $J_z/2 < h \lesssim J_z$, the spin-wave description, which assumes a polarized ground state, would be unstable.

The classical and quantum dispersions at their respective critical fields have the same functional form (sinusoidal), but they predict different dispersion bandwidths, i.e., $\hbar\omega(h = h_c) = J_z |\sin \frac{\pi l}{2}|$ compared to $\hbar\omega^{\rm cl}(h = h_c^{\rm cl}) = \sqrt{2} J_z |\sin \frac{\pi l}{2}|$, so the spin-wave formula Eq. (11) can be used to "fit" the quantum dispersion at the actual critical field h_c, but using a renormalized exchange $\tilde{J}_z = J_z/\sqrt{2}$ and a renormalized Zeeman energy $\tilde{h} = \sqrt{2}h$, i.e., the "fitted" exchange would appear ∼30% smaller than the actual value and one would have to use an artificially larger Zeeman term. For fields above h_c, the classical and quantum dispersions do not have the same functional form, but one can approximately "fit" the quantum dispersion (12) with a classical relation (11) with renormalization factors for J_z and h that progressively tend to unity in the limit of very high field, $h/J_z \to \infty$.

Based on the above discussion, we propose that quantum renormalizations of the dispersion not captured by a spin-wave approach in the region of transverse fields slightly above the critical field are responsible for the apparently smaller dispersion bandwidth than predicted. We note that the empirically extracted renormalization at 9 T is smaller compared to 7 T. This is consistent with the expectation that quantum renormalization of the bandwidth decreases upon increasing field closer to the high-field limit. Future experiments at sufficiently large fields could provide a test for where renormalization effects become negligible and the classical and quantum descriptions become equivalent.

VI. CONCLUSIONS

We have reported a comprehensive study of the magnetic dispersion relations using inelastic neutron scattering in the quasi-1D Ising ferromagnet $CoNb_2O_6$ in the quantum paramagnetic phase in a high transverse magnetic field. The spectrum is dominated by a sharp mode, as expected for coherently propagating spin-flip quasiparticles. In addition to the main dispersive mode, much weaker intensity shadow modes were also observed and attributed to the enlargement of the magnetic unit cell due to the buckling of the magnetic chains and the alternating rotation of Ising axes between chains. The largest dispersion is observed along the chain direction l, with clear modulations in the dispersion along h and k at the lowest energies due to the interchain couplings, which form an isosceles triangular lattice geometry. The observed dispersions have been parametrized by a phenomenological spin-flip hopping model and also by a linear spin-wave model. Differences in the observed dispersion bandwidth along the chain direction and spin-wave prediction using estimated exchange values from analysis of zero-field dispersions are attributed to strong quantum renormalization effects of the dispersion relation in the quantum paramagnetic phase not captured by a linear spin-wave approach for fields slightly above the critical field, where quantum fluctuations in the ground state are still significant.

ACKNOWLEDGMENTS

We acknowledge very useful discussions with F. H. L. Essler and N. J. Robinson. I.C. and R.C. acknowledge support from the EPSRC Grant No. EP/H014934/1. J.D.T. was supported by the University of Oxford Clarendon Fund Scholarship and NSERC of Canada. This work utilized facilities supported in part by the National Science Foundation under Agreement No. DMR-0944772. We acknowledge STFC (UK) and the National Institute of Standards and Technology, US Department of Commerce for providing the neutron research facilities used in this work, and we thank the technical staff at those facilities for cryogenics support. We acknowledge collaboration with E. M. Wheeler on preliminary measurements of magnetic excitations at lower applied magnetic fields at the Helmholtz-Zentrum Berlin [19].

APPENDIX: DYNAMICAL CORRELATIONS IN THE SPIN-WAVE MODEL

For completeness, we outline here the derivation of the dynamical structure factor for the spin-wave model for the Hamiltonian in Eq. (2) in the the limit of high magnetic fields B, where the mean-field ground state has fully polarized spins along the field direction. It is useful to relabel the axes as $(x,y,z) = (z',-y',x')$ such that the equilibrium spin direction is along z' (and the Ising axis is along x'). Using a Holstein-Primakoff transformation to spin deviation operators (for each spin site $S^{z'} = S - a^\dagger a, S^+ \simeq \sqrt{2S}a, S^- \simeq \sqrt{2S}a^\dagger$), the leading form of the Hamiltonian expansion in terms of spin-wave operators is $\mathcal{H} = NE_{\rm MF}(1+1/S) + \sum_{\boldsymbol{k}} \mathsf{X}^\dagger \mathsf{H} \mathsf{X}$. The first term contains $E_{\rm MF}$, the mean-field ground-state energy normalized to the number of sites (N), and the second term is a quadratic form of Bose operators written in a matrix form using the operator basis $\mathsf{X}^\dagger = [a^\dagger_{\boldsymbol{k}}, a_{-\boldsymbol{k}}]$ and the Hamiltonian matrix

$$\mathsf{H} = \frac{1}{2}\begin{bmatrix} A_{\boldsymbol{k}} & B_{\boldsymbol{k}} \\ B_{\boldsymbol{k}} & A_{\boldsymbol{k}} \end{bmatrix}. \tag{A1}$$

Here $a^\dagger_{\boldsymbol{k}} = \frac{1}{\sqrt{N}} \sum_{\boldsymbol{r}} e^{-i\boldsymbol{r}\cdot\boldsymbol{k}} a^\dagger_{\boldsymbol{r}}$ creates a spin wave of momentum $\boldsymbol{k}$ (the sum extends over all spin sites $\boldsymbol{r}$). Expressions for $A_{\boldsymbol{k}}$ and $B_{\boldsymbol{k}}$ (both real) are given in Eq. (4). Diagonalizing the quadratic Hamiltonian form using standard methods [20] gives the dispersion relation $\hbar\omega_{\boldsymbol{k}} = \sqrt{A^2_{\boldsymbol{k}} - B^2_{\boldsymbol{k}}}$, and the transformation between the original basis and the normal magnon basis, $\mathsf{X}'^\dagger = [\alpha^\dagger_{\boldsymbol{k}}, \alpha_{-\boldsymbol{k}}]$, $\mathsf{X} = \mathsf{S}\mathsf{X}'$, is obtained as

$$\mathsf{S} = \begin{bmatrix} u_{\boldsymbol{k}} & -v_{\boldsymbol{k}} \\ -v_{\boldsymbol{k}} & u_{\boldsymbol{k}} \end{bmatrix}, \tag{A2}$$

where $u_{\boldsymbol{k}} = \cosh\theta_{\boldsymbol{k}}$, $v_{\boldsymbol{k}} = \sinh\theta_{\boldsymbol{k}}$, and $\tanh 2\theta_{\boldsymbol{k}} = B_{\boldsymbol{k}}/A_{\boldsymbol{k}}$. In the normal magnon basis, the Fourier-transformed spin operator along the Ising axis is $S^{x'}_{\boldsymbol{k}} = \sqrt{\frac{S}{2}}(u_{\boldsymbol{k}} - v_{\boldsymbol{k}})[\alpha_{\boldsymbol{k}} + \alpha^\dagger_{-\boldsymbol{k}}]$. From this, the dynamical correlations along the x' axis are obtained as $S^{x'x'}(\boldsymbol{k},E) = \frac{S}{2}|u_{\boldsymbol{k}} - v_{\boldsymbol{k}}|^2 \delta(E - \hbar\omega_{\boldsymbol{k}}) = \frac{S}{2}\frac{A_{\boldsymbol{k}} - B_{\boldsymbol{k}}}{\hbar\omega_{\boldsymbol{k}}} \delta(E - \hbar\omega_{\boldsymbol{k}})$. Similarly, $S^{y'y'}(\boldsymbol{k},E) = \frac{S}{2}|u_{\boldsymbol{k}} + v_{\boldsymbol{k}}|^2 \delta(E - \hbar\omega_{\boldsymbol{k}}) = \frac{S}{2}\frac{A_{\boldsymbol{k}} + B_{\boldsymbol{k}}}{\hbar\omega_{\boldsymbol{k}}} \delta(E - \hbar\omega_{\boldsymbol{k}})$, giving the expressions listed in the text after Eq. (6).

[1] S. Sachdev, *Quantum Phase Transitions* (Cambridge University Press, London, 1999), Chap. 4.

[2] P. Pfeuty, Ann. Phys. (NY) **57**, 79 (1970).

[3] R. Coldea, D. A. Tennant, E. M. Wheeler, E. Wawrzynska, D. Prabhakaran, M. Telling, K. Habicht, P. Smeibidl, and K. Kiefer, Science **327**, 177 (2010).

[4] C. M. Morris, R. Valdés Aguilar, A. Ghosh, S. M. Koohpayeh, J. Krizan, R. J. Cava, O. Tchernyshyov, T. M. McQueen, and N. P. Armitage, Phys. Rev. Lett. **112**, 137403 (2014).

[5] A. B. Zamolodchikov, Int. J. Mod. Phys. A **4**, 4235 (1989).

[6] S. Lee, R. K. Kaul, and L. Balents, Nat. Phys. **6**, 702 (2010).

[7] S. T. Carr and A. M. Tsvelik, Phys. Rev. Lett. **90**, 177206 (2003).

[8] C. Heid, H. Weitzel, P. Burlet, M. Bonnet, W. Gonschorek, T. Vogt, J. Norwig, and H. Fuess, J. Magn. Magn. Mater. **151**, 123 (1995).

[9] C. Heid, H. Weitzel, P. Burlet, M. Winkelmann, H. Ehrenberg, and H. Fuess, Physica B **234-236**, 574 (1997).

[10] P. Bak and J. von Boehm, Phys. Rev. B **21**, 5297 (1980).

[11] D. Prabhakaran, F. Wondre, and A. Boothroyd, J. Cryst. Growth **250**, 72 (2003).

[12] J. A. Rodriguez, D. M. Adler, P. C. Brand, C. Broholm, J. C. Cook, C. Brocker, R. Hammond, Z. Huang, P. Hundertmark, J. W. Lynn, N. C. Maliszewskyj, J. Moyer, J. Orndorff, D. Pierce, T. D. Pike, G. Scharfstein, S. A. Smee, and R. Vilaseca, Meas. Sci. Technol. **19**, 034023 (2008).

[13] R. Bewley, J. Taylor, and S. Bennington., Nucl. Instrum. Methods Phys. Res. A **637**, 128 (2011).

[14] T. G. Perring, R. A. Ewings, and J. V. Duijn, http://horace.isis.rl.ac.uk.

[15] Although interactions between S^x and S^y spin components are allowed between further neighbors, we expect the resulting exchanges to be small enough to be neglected for the purposes of characterizing the dispersion relations in $CoNb_2O_6$.

[16] J. A. Kjäll, F. Pollmann, and J. E. Moore, Phys. Rev. B **83**, 020407 (2011).

[17] N. J. Robinson, F. H. L. Essler, I. Cabrera, and R. Coldea, arXiv:1407.2794.

[18] S. B. Ruthkevich, J. Stat. Mech. (2010) P07015.

[19] E. M. da Silva Wheeler, Ph.D. thesis, University of Oxford, 2007.

[20] R. M. White, M. Sparksparks, and I. Ortenburger, Phys. Rev. **139**, A450 (1965).